

Article

# Entropy Generation and Thermal Radiation Impact on Magneto-Convective Flow of Heat-Generating Hybrid Nano-Liquid in a Non-Darcy Porous Medium with Non-Uniform Heat Flux

Nora M. Albqmi <sup>1,3</sup> and Sivasankaran Sivanandam <sup>1,2,\*</sup>

<sup>1</sup> Mathematical Modelling and Applied Computation Research Group, Department of Mathematics, King Abdulaziz University, Jeddah 21589, Saudi Arabia; nora.m.albqmi@gmail.com

<sup>2</sup> Department of Mathematics, Saveetha School of Engineering, SIMATS, Chennai 602105, India

<sup>3</sup> Department of Mathematics, Taif University, Taif 21944, Saudi Arabia

\* Correspondence: sd.siva@yahoo.com

**Abstract:** The principal objective of the study is to examine the impact of thermal radiation and entropy generation on the magnetohydrodynamic hybrid nano-fluid,  $\text{Al}_2\text{O}_3/\text{H}_2\text{O}$ , flow in a Darcy–Forchheimer porous medium with variable heat flux when subjected to an electric field. Investigating the impact of thermal radiation and non-uniform heat flux on the hybrid nano-liquid magnetohydrodynamic flow in a non-Darcy porous environment produces novel and insightful findings. Thus, the goal of the current study is to investigate this. The non-linear governing equation can be viewed as a set of ordinary differential equations by applying the proper transformations. The resultant dimensionless model is numerically solved in Matlab using the *bvp4c* command. We obtain numerical results for the temperature and velocity distributions, skin friction, and local Nusselt number across a broad range of controlling parameters. We found a significant degree of agreement with other research that has been compared with the literature. The results show that an increase in the Reynolds and Brinckmann numbers corresponds to an increase in entropy production. Furthermore, a high electric field accelerates fluid velocity, whereas the unsteadiness parameter and the presence of a magnetic field slow it down. This study is beneficial to other researchers as well as technical applications in thermal science because it discusses the factors that lead to the working hybrid nano-liquid thermal enhancement.

**Keywords:** entropy generation; hybrid nano-fluid; non-uniform heat-flux; porous medium; MHD; stretching sheet



**Citation:** Albqmi, N.M.; Sivanandam, S. Entropy Generation and Thermal Radiation Impact on Magneto-Convective Flow of Heat-Generating Hybrid Nano-Liquid in a Non-Darcy Porous Medium with Non-Uniform Heat Flux. *Computation* **2024**, *12*, 43. <https://doi.org/10.3390/computation12030043>

Received: 31 December 2023

Revised: 11 February 2024

Accepted: 26 February 2024

Published: 29 February 2024



**Copyright:** © 2024 by the authors. Licensee MDPI, Basel, Switzerland. This article is an open access article distributed under the terms and conditions of the Creative Commons Attribution (CC BY) license (<https://creativecommons.org/licenses/by/4.0/>).

## 1. Introduction

Efficient heat transfer has been of increasing interest to engineers for decades. Scientists have thus laboured ceaselessly to increase heat transmission and thermal conductivity. The frictional loss, pressure dips, and pumping power for heat transfer fluid are all things they are working to minimise. As a result, scientists have developed nano-fluids, a novel kind of heat transfer fluid with enhanced thermal characteristics. Nano-fluids may be made with or without stabilising by dispersing nano-particles in a base fluid like water, ethylene glycol, etc. Experimental and numerical studies of nano-fluid properties in a variety of flow regimes have been conducted in recent years. Alizadeh [1] investigated the heat transmission and flow of a magnetohydrodynamic micro-polar nano-liquid in a channel with permeable walls and the effect of thermal radiation. Mondal [2] studied heat and mass transfer in a nano-fluid flow that includes viscous dissipation, heat generation, and a decreasing axisymmetric sheet. Parveen [3] conducted a numerical study of the effects of a uniform vertical magnetic field on the entropy production and heat and mass transfer during the steady, double-diffusive, natural convection of a water– $\text{Al}_2\text{O}_3$  nano-fluid within

a wavy-walled chamber with a central heater. Li [4] used computational methods to examine the heat generation/absorption and mass suction in a magnetohydrodynamic Williamson nano-fluid flow across an exponentially porous stretched surface. Yu [5] investigated the impact of generalised slip effects on a three-dimensional stagnation-point flow caused by copper oxide nano-particles into the underlying working fluid (water) across a horizontal plane surface embedded in a porous medium. Two nano-fluids were investigated by Reddy [6] as they floated buoyantly in a porous annular region undergoing a convective flow. Khan [7] demonstrated the dynamics of a nano-fluid subject to a convective boundary condition, including the flow and heat transfer generated by a non-linearly expanding and contracting sheet.

Compared to traditional nano-fluids, hybrid nano-fluids showed improved thermal conductivity properties; the addition of hybrid nano-particle may dramatically boost the base fluid's thermal conductivity. Nano-fluids (both hybrid and simple) were studied by Hayat [8] in terms of their heat transfer rates across a stretched sheet when subjected to radiation, heat production, and chemical reactions. They found that the temperature of the hybrid nano-fluid (Ag-CuO/H<sub>2</sub>O) was greater than that of a regular nano-fluid. Nadeem [9] investigated the behaviour of a hybrid nano-fluid in three dimensions, both with and without thermal slip effects. Kaska [10] looked at how the hybrid nano-fluid of alumina nitride and alumina oxide affected convective thermal transport. Khan [11] conducted a theoretical investigation on the combined effects of shrinking/stretching surfaces on heat transfer in a mixed convective radiative flow. Rajesh [12] investigated how hybrid nano-fluids affect unsteady magnetohydrodynamic flow and heat transport via a vertical plate. Mishra [13] looked into the effects of chemical reactions on the flow of two types of hybrid nano-fluids, measuring temperature and concentration changes.

In the fields of metallurgy and chemical engineering, the flow through a stretched sheet is significant for many crucial engineering applications. Crane [14] studied fluid dynamics on elastic surfaces and found some interesting results. Scientists have investigated the flow issue caused by overstretching sheets when subjected to various effects. In the situation of non-steady flow, Govardhan [15] published a boundary layer study of magnetohydrodynamics and radiation effects on the mixed convection flow of incompressible micro-polar fluid across a stretched sheet. In the presence of suction/injection, two-dimensional steady magnetohydrodynamics allowed Naramgari [16] to examine the effect of heat radiation and chemical reactions on the flow of a nano-fluid via a permeable stretched sheet. Ibrahim [17] discovered numerical findings for a nano-fluid's flow and heat transmission across a stretched sheet in two-dimensional steady-state magnetohydrodynamics. Mohammadein [18] examines the influence of non-linear thermal radiation on the boundary layer flow of a nano-fluid in two dimensions towards a linearly extending sheet at the stagnation point of forced convection. During his research, Kho [19] analysed the effects of slip circumstances on the heat transfer and flow of a Williamson nano-fluid across a stretched sheet. The hydrodynamic stagnation point flow of Sisko nano-fluid across a linearly stretched sheet was shown to be affected by thermo-diffusion by Pal [20]. Unsteady magnetohydrodynamic stagnation-point flow caused by an exponentially permeable stretched sheet was the subject of Zainal's [21] numerical investigation. Finally, Tawade [22] studied the temperature and concentration boundary layer flow of a Casson nano-fluid across a linearly stretched sheet, paying particular attention to the role played by thermophoresis and Brownian motion.

Conducting fluids and magnetic fields have an effect on a wide variety of industrial machinery, from pumps to plasma and magnetohydrodynamics generators. Daniel [23,24] investigated the effect of heat on the movement of electrically charged nano-fluids using magnetohydrodynamics. Golbal [25] spoke on how a stretched porous sheet affects the intensity of electrical, magnetic, and viscous dissipation in higher-order chemical reactions. Niranjana [26] performed an analytical and numerical investigation into the impact of slip and radiation on the magneto-convection flow of a chemically reacting fluid approaching a stagnation point towards a vertical plate embedded in a porous medium. The most

important discovery is that reducing a chemical reaction parameter causes an increase in velocity and concentration. Increasing the chemical reaction parameter also reduces skin friction. In the presence of magnetohydrodynamics, heat generation/absorption, and chemical reactions, Sivasankaran [27] demonstrated the Newtonian heating and slide effect on a mixed convection flow close to a stagnation point in a porous medium with thermal radiation. Niranjana [28] studied the influence of diffusion–thermal and thermal–diffusion on the steady magneto-convection flow of an incompressible viscous fluid across a vertical plate at a stagnation point in the presence of slip, chemical reactions, and radiation. To learn how thermal radiation and the Darcy number affect the buoyant convection flow of Casson fluid in a non-Darcian porous square box heated non-uniformly using the control volume approach, Sivasankaran [29] ran a numerical simulation. Using discrete heating and cooling, Sivasankaran [30] investigated the rate of change in thermal and flow transfers within an enclosed box due to the effects of thermal radiation and convective flow caused by buoyant forces. Mallawi [31] elaborated on how thermal radiation modifies the effects of the double stratification and double heat flux of a non-Newtonian fluid in a Riga plate. The unstable stagnation-point flow of a Cu–Al<sub>2</sub>O<sub>3</sub>/H<sub>2</sub>O hybrid nano-fluid towards a radially diminishing Riga surface with heat radiation was numerically investigated by Khashi'ie [32]. Zainal [33] investigated the fluctuating flow at the stagnation point in the direction of a stretching and contracting Riga plate of Al<sub>2</sub>O<sub>3</sub>-Cu/H<sub>2</sub>O and the effect of heat radiation on the motion of the boundary layer. According to their findings, the thermal radiation impact of Al<sub>2</sub>O<sub>3</sub>-Cu/H<sub>2</sub>O reduces the heat transfer conductivity by lowering the local Nusselt number.

Absorbing or generating heat is the primary cause of internal temperature variation. As a result, heat sources and sinks play a crucial role in the refrigeration process, with freezers and air conditioners serving as typical examples. In addition, there are several HVAC systems that include these heat pumps. Thus, it is believed that heat production and absorption are space–temperature-related. Bhuvaneshwari [34] investigated the effects of radiation on heat transport by natural convection on a semi-infinitely sloped surface. An unstable mixed convective boundary layer flow of a magneto-micro-polar fluid across a stretching/shrinking sheet with viscous dissipation and suction/injection was studied by Sandeep [35], who looked at the effects of a non-uniform heat source/sink, mass transfer, and chemical reaction. Karthikeyan [36] examined the influence of viscosity and variable thermal conductivity on mixed convective heat and mass transport through a vertical wavy surface embedded in a fluid-saturated porous medium with Dufour and Soret effects. Ali [37] investigated the flow and heat transmission of two different stress fluids across an oscillating stretched sheet with a heat source and a heat sink. Irfan [38] investigated the flow and heat transmission properties of an unstable three-dimensional Carreau nano-fluid from a heat source/sink perspective. Cheong [39] investigated the effects of internal heat production or absorption on the natural convective flow and heat transmission in a sinusoidally heated, wavy porous cavity. Khan [40] achieved the heat source/sink qualities and nano-particles' mass flux conditions for Maxwell nano-fluids in two dimensions under the effect of a stretching cylinder. Using a Riga plate as a non-uniform heat source/sink, Ragupathi [41] demonstrated the numerical analysis of the steady, three-dimensional flow of (H<sub>2</sub>O/NaC<sub>6</sub>H<sub>9</sub>O<sub>7</sub>) nano-fluids with (Fe<sub>3</sub>O<sub>4</sub>/Al<sub>2</sub>O<sub>3</sub>) nano-particles. Heat transfer in the boundary layer flow across a stretched porous surface subjected to a heat source/sink and magnetic field was the subject of Agrawal's [42] research. In the presence of a changing source/sink and Newtonian heating in a rotating flow over a deformable surface, Chu [43] studied the magnetohydrodynamics of a Maxwell nano-fluid, including gyrotactic microorganisms and higher-order chemical processes. By a chemically sensitive method, Bhuvaneshwari [44] analysed the effects of radiation and cross-diffusion on an unsteady stream moving over an extended porous matrix. Yesodha [45] looked into the role of nano-fluids in chemical reactions on stretched sheets in three-dimensional flow. With several slips, a heat source/sink, and non-linear thermal radiation

all in play, Gautam [46] demonstrated a comparative study of the flow of Maxwell and Casson fluids in bio-convective magnetohydrodynamics.

The idea of entropy in the thermodynamic system was specified by Rudolf Clausius in the 1850s. The thermal energy amount is the quantity of heat produced by a body at a given temperature, and it is too high for use in real tanks. Entropy creation refers to the amount of entropy created by processes that cannot be reversed. It is the determining factor in how the thermodynamic system operates. Convective heat exchange was the topic of Bejan's [47,48] discussion on entropy production. Entropy generation has become more important in many technological fields, including heat converters, porous media, electronic cooling, gas turbines, and combustion. Entropy creation in the flow of a magnetohydrodynamic viscous nano-fluid through a permeable wedge was the topic of Goqo's [49] presentation. They discovered that, depending on the kind of convection in the flow, the magnetic field tends to induce a drag force, revealing the fluid motion and either lowering or raising the temperature and concentration. The convective flow of a Sisko nano-fluid across a flexible rotating disc was investigated by Ijaz [50], who looked for ways to optimise entropy production and determine the activation energy. Abbas [51] investigated the rate at which entropy is produced by a viscous fluid flowing through a vertical permeable channel subjected to heat radiation. Ghaffari [52] investigated the heat transmission and entropy generating in a power-law nano-fluid flow towards the stagnation point inside the boundary layer over a deformable spinning disc embedded in porous media. In this study, Ibrahim [53] examined the influence of a high-order velocity slip flow, passive and active control conditions, non-heat Fourier's flux, and non-mass Fick's flux theory on the entropy generation analysis of 3D mixed convection flow of pair stress nano-fluid. Alzahrani [54] analysed the influence of aspect ratio and entropy generation on the buoyant convective flow of Casson fluid within a rectangular box. Sivasankran [55] investigated the direction of a moving wall, thermal radiation, and entropy on combined convective steam and the energy transfer of a nano-fluid in an enclosed box with a driven lid. Within the two parallel discs, Agrawal [56] examined the compressing flow of a hybrid nano-fluid. Given buoyancy force, Bai [57] discussed the effect of entropy generation on the unsteady flow of an upper-convected Maxwell nano-fluid past a wedge embedded in a porous medium.

To the best of the authors' knowledge, no research has been conducted on how thermal radiation and non-uniform heat flux affect the convective flow of heat-generating hybrid nano-liquids in a non-Darcy porous medium in the presence of a uniform external magnetic field. This has encouraged us to investigate this using entropy generation, which has not been reported thus far based on a careful review of the literature. In this concept, the basic liquid, water, is combined with copper and aluminium oxide to create the hybrid nano-liquid. The nano-particles of metallic oxides, such as  $\text{Al}_2\text{O}_3$ ,  $\text{SiO}_2$ ,  $\text{ZnO}$ , and  $\text{TiO}_2$ , are readily soluble in base fluids, with  $\text{Al}_2\text{O}_3$  possessing the highest thermal properties among these metal oxides. Furthermore, it is commonly recognised that metallic nano-particles that have been refined, like copper, have high aspect ratios, high thermal conductivities, and low specific gravities. However, the combination of copper (Cu) and aluminium oxide ( $\text{Al}_2\text{O}_3$ ) tends to stabilise nano-liquids with superior thermal properties for an extended period of time. Numerous combinations of study parameters have been used to thoroughly examine the effects of thermal radiation, heat generation, and non-uniform heat flow on an electrical magnetohydrodynamic hybrid nano-fluid over a linearly expanding sheet with entropy generation. The study is useful for the cooling of electronic equipment, food processing, material processing, and the plastic and chemical industries.

## 2. Equations and Physical Formulation

We examine the laminar flow of an incompressible, electrically conducting hybrid nano-fluid ( $\text{Al}_2\text{O}_3\text{-Cu}/\text{H}_2\text{O}$ ) undergoing 2D unsteady magnetohydrodynamic mixed convection on a stretched sheet. The sheet is stretching spontaneously from both sides; therefore, the velocity varies with time and place. In a rectangular coordinate system, the

stretched sheet is the x-axis and the normal y-axis, and the flow is limited to the area where y is greater than zero. The application of the magnetic and electrical fields is perpendicular to the fluid’s flow. The Darcy–Forchheimer model is used to model isotropic porous media. The local liquid and porous matrix are in thermal equilibrium. The surface temperature,  $T_w(x, t)$ , is thought to be higher than the surrounding (free-stream) temperature,  $T_\infty$ , in the immediate vicinity, (See Table 1 for all symbols and abbreviations). In this case, the magnetic induction and Hall current are disregarded due to the low magnetic Reynolds number.

**Table 1.** Abbreviations.

$a, b$	Constants	$A$	Space-dependent coefficient
$B$	Temperature-dependent coefficient	$Br$	Brinkman number
$B_0$	Strength of magnetic field ( $T$ )	$c_p$	Heat capacity ( $Jkg^{-1}K^{-1}$ )
$C_f$	Skin friction coefficient	$E_0$	Strength of electric field $N/C$
$E_1$	Electric field parameter	$F$	Local inertia coefficient
$Fr$	Forchheimer coefficient	$g$	Acceleration due to gravity ( $ms^{-2}$ )
$K^*$	Porous medium permeability	$k^*$	Mean absorption coefficient
$M$	Magnetic field parameter	$n$	Shape factor
$Nu$	Nusselt number	$P$	Fluid pressure ( $Pa$ )
$Pr$	Prandtl number	$q_r$	Radiative heat flux ( $Wm^{-2}$ )
$Rd$	Radiation number	$Re$	Reynolds number
$s$	Suction/injection	$T$	Fluid temperature ( $K$ )
$T_\infty$	Free stream temperature ( $K$ )	$T_w$	Surface temperature ( $K$ )
$U, V$	$x, y$ Velocity component	$U_w$	Stretching sheet velocity ( $ms^{-1}$ )
$V_w$	Wall mass transfer		
<b>Greek symbols</b>			
$\alpha^*$	Drag inverse number	$\beta$	Thermal expansion ( $K^{-1}$ )
$\delta$	Unsteadiness parameter	$\kappa$	Thermal conductivity ( $Wm^{-1}K^{-1}$ )
$\lambda$	Mixed convection parameter	$\mu$	Dynamic viscosity ( $kgm^{-1}s^{-1}$ )
$\nu$	Kinematic viscosity ( $m^2s^{-1}$ )	$\rho$	Density ( $kgm^{-3}$ )
$\sigma^*$	Stefan–Boltzmann constant ( $Wm^{-2}K^{-4}$ )	$\sigma$	Electric conductivity ( $Sm^{-1}$ )
$\phi_1$	Nano-particles volume fraction	$\phi_2$	Nano-particles volume fraction
$\psi$	Stream function	$\Omega$	Dimensionless temperature ratio
<b>Subscripts</b>			
$f$	Base fluid	$nf$	Nano-fluid
$hnf$	Hybrid nano-fluid	$s_1$	First solid nano-particle
$s_2$	Second nano-particle		

The following equations for mass, momentum, and heat under these conditions control the model (see Figure 1) [58]:

$$U_x + V_y = 0 \tag{1}$$

$$U_t + UU_x + VU_y = -\frac{1}{\rho_{hnf}}P_x + v_{hnf}(U_{xx} + U_{yy}) + \frac{\sigma_{hnf}}{\rho_{hnf}}(EB - B^2U) + \frac{(\rho\beta)_{hnf}}{\rho_{hnf}}(T - T_\infty)g - \frac{v_{hnf}}{K^*}U - FrU^2 \tag{2}$$

$$V_t + UV_x + VV_y = -\frac{1}{\rho_{hnf}}P_y + v_{hnf}(V_{xx} + V_{yy}) \tag{3}$$

$$T_t + UT_x + VT_y = \alpha_{hnf}(T_{xx} + T_{yy}) - \frac{1}{(\rho c_p)_{hnf}}[(q_r)_y + q''' + \mu_{hnf}(2(U_x^2 + V_y^2) + (U_y + V_x)^2)] \tag{4}$$

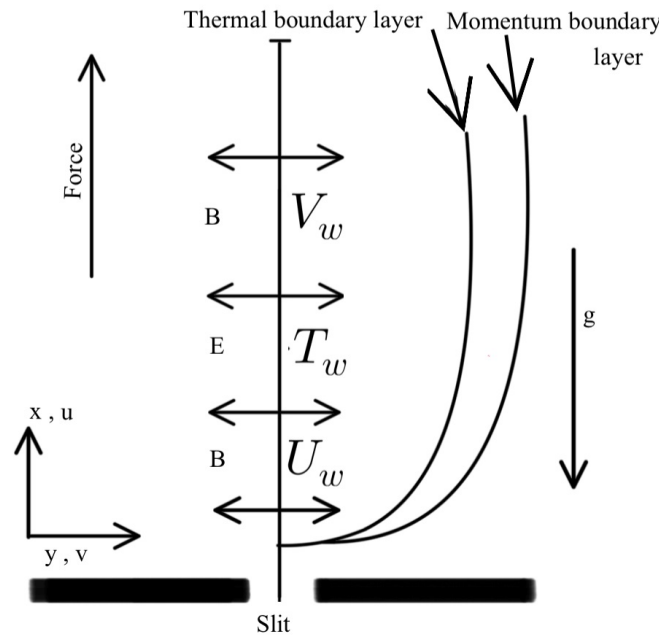


Figure 1. Coordinate system and formulation.

The boundary conditions for the physical model are [58]

$$\begin{aligned} U = U_w(x, t) \quad V = V_w(x, t) \quad T = T_w(x, t) \quad \text{when } y = 0 \\ U \rightarrow 0 \quad T \rightarrow T_\infty \quad \text{at } y \rightarrow \infty \end{aligned} \quad (5)$$

The linear stretching sheet velocity is represented by  $U_w(x, t) = \frac{bx}{-(at-1)}$  ( $b$  and  $a$  are positive dimensional constants with a dimension of time and  $-(at-1) > 0$ ), and mass transfer at the wall is denoted by  $V_w(x, t) = \frac{V_0}{\sqrt{-(at-1)}}$ , where  $V_w \geq 0$  means suction and  $V_w \leq 0$  means injection. The strength of an electric field is given by  $E = \frac{E_0}{\sqrt{-(at-1)}}$ , while the strength of a magnetic field is given by  $B = \frac{B_0}{\sqrt{-(at-1)}}$ . The variable heat production/absorption, denoted by  $q'''$  in Equation (4), is stated as

$$q''' = \frac{\kappa_{hmf} U_w}{xv_{hmf}} [A(T_w - T_\infty f') + (T - T_\infty)B] \quad (6)$$

If  $(A, B) > 0$ , then the flow generates heat, and if  $(A, B) < 0$ , then the flow absorbs heat. The Rosseland's approach gives

$$q_r = -\frac{4\sigma^*}{3k^*} T_y^4 \quad (7)$$

where  $\sigma^*$  is a coefficient of Stefan–Boltzmann and  $k^*$  is the mean absorption coefficient. If we use Taylor's expansion of  $T^4$  around  $T_\infty$  and disregard higher-order terms, we obtain

$$T^4 \cong 4T_\infty^3 T - 3T_\infty^4 \quad (8)$$

Inserting Equations (7) and (8) into Equation (4) yields

$$\begin{aligned} (\rho c_p)_{hmf} (T_t + UT_x + VT_y) = \kappa_{hmf} (T_{xx} + T_{yy}) + \frac{16\sigma^* T_\infty^3}{3k^*} T_{yy} \\ + \mu_{hmf} U_y^2 + V_y^2 + q''' \end{aligned} \quad (9)$$

As a result of utilising scale analysis and boundary layer approximations,

$$\begin{aligned}
 U &\gg V \\
 U_y &\gg V_x, U_x, V_y, V_t \\
 T_y &\gg T_x \\
 P_y &= 0
 \end{aligned}
 \tag{10}$$

After performing a boundary layer analysis, the following set of equations was derived:

$$U_x + V_y = 0 \tag{11}$$

$$\begin{aligned}
 U_t + UU_x + VU_y &= \nu_{hmf} U_{yy} + \frac{\sigma_{hmf}}{\rho_{hmf}} (EB - B^2U) \\
 &+ \frac{(\rho\beta)_{hmf}}{\rho_{hmf}} (T - T_\infty)g - \frac{\nu_{hmf}}{K^*} U - FrU^2
 \end{aligned}
 \tag{12}$$

$$\begin{aligned}
 T_t + UT_x + VT_y &= \alpha_{hmf} T_{yy} + \frac{1}{(\rho c_p)_{hmf}} \left( \frac{16T_\infty^3 \sigma^*}{3k^*} T_{yy} \right) \\
 &+ \frac{\mu_{hmf}}{(\rho c_p)_{hmf}} U_y^2 + \frac{1}{(\rho c_p)_{hmf}} \frac{\kappa_{hmf} U_w}{x\nu_{hmf}} [Af'(T_w - T_\infty) + (T - T_\infty)]
 \end{aligned}
 \tag{13}$$

### 3. Method of Solution

We now add the following dimensionless quantities; similarity transformations simplify the mathematical examination of the problem [58]

$$\begin{aligned}
 \eta = y \left( \frac{b}{(1-at)\nu_f} \right)^{\frac{1}{2}}, \quad \theta = \frac{T - T_\infty}{T_w - T_\infty}, \quad \psi = \left( \frac{\nu_f b}{1-at} \right)^{\frac{1}{2}} \\
 T_w(x, t) = \frac{xb}{2(1-at)^2\nu_f} T_0 + T_\infty
 \end{aligned}
 \tag{14}$$

The definition of the stream function is

$$U = \psi_y, \quad V = -\psi_x \tag{15}$$

when the additional variables (14) and (15) are substituted into Equations (11) through to (13), the resulting set of ordinary differential equations is as follows:

$$\begin{aligned}
 A_1 f'''' + A_2 (f''f - f'^2(1 + Fr) - \delta \left( \frac{\eta}{2} f'' + f' \right)) + A_3 M(E_1 - f') \\
 + A_4 \lambda \theta - A_1 \alpha^* f' = 0
 \end{aligned}
 \tag{16}$$

$$\begin{aligned}
 \theta'' \left( A_5 + \frac{4}{3} Rd \right) + A_6 Pr (\theta'f - \theta f' - \left( \frac{\eta}{2} \theta' + 2\theta \right) \delta) \\
 + A_1 Br f'^2 + \frac{A_2 A_5}{A_1} (Af' + B\theta) = 0
 \end{aligned}
 \tag{17}$$

The  $A_i$ s ( $i = 1, 2, 3, 4, 5, 6$ ) in the above equation are stated as

$$A_1 = (1 - \phi_1)^{-2.5} (1 - \phi_2)^{-2.5} \tag{18}$$

$$A_2 = \left[ (1 - \phi_1) + \phi_1 \frac{\rho_{s1}}{\rho_f} \right] (1 - \phi_2) + \frac{\rho_{s2}}{\rho_f} \phi_2 \tag{19}$$

$$A_3 = \frac{\sigma_{s_2} + 2\phi_2(\sigma_{s_2} - \sigma_{nf}) + 2\sigma_{nf}}{\sigma_{s_2} + 2\sigma_{nf} + \phi_2(\sigma_{nf} - \sigma_{s_2})} \times \frac{\sigma_{s_1} + 2\phi_1(\sigma_{s_1} - \sigma_f) + 2\sigma_f}{\sigma_{s_1} + 2\sigma_f + \phi_1(\sigma_f - \sigma_{s_1})} \quad (20)$$

$$A_4 = \left[ (1 - \phi_1) + \phi_1 \frac{(\rho\beta)_{s_1}}{(\rho\beta)_f} \right] (1 - \phi_2) + \frac{(\rho\beta)_{s_2}}{(\rho\beta)_f} \phi_2 \quad (21)$$

$$A_5 = \frac{\kappa_{s_2} - (n - 1)(\kappa_{nf} - \kappa_{s_2})\phi_2 + (n - 1)\kappa_{nf}}{\kappa_{s_2} + (\kappa_{nf} - \kappa_{s_2})\phi_2 + (n - 1)\kappa_{nf}} \times \frac{\kappa_{s_1} - (n - 1)(\kappa_f - \kappa_{s_1})\phi_1 + (n - 1)\kappa_f}{\kappa_{s_1} + (\kappa_f - \kappa_{s_1})\phi_1 + (n - 1)\kappa_f} \quad (22)$$

$$A_6 = \left[ (1 - \phi_1) + \phi_1 \frac{(\rho c_p)_{s_1}}{(\rho c_p)_f} \right] (1 - \phi_2) + \frac{(\rho c_p)_{s_2}}{(\rho c_p)_f} \phi_2 \quad (23)$$

By adjusting boundary conditions, we obtain

$$\begin{aligned} f(\eta) = s, \quad f'(\eta) = 1, \quad \theta(\eta) = 1 \quad \text{when } \eta = 0 \\ f'(\eta) = 0, \quad \theta(\eta) = 0 \quad \text{as } \eta = \infty \end{aligned} \quad (24)$$

Differentiation with regard to  $\eta$  is represented by prime. The physical parameter in the aforementioned governing model is given by

$$\begin{aligned} M = \frac{\sigma_f B_0^2}{b\rho_f}, \quad Gr = \frac{g\beta_f(T_w - T_\infty)x^3}{\nu_f^2}, \quad \delta = \frac{a}{b}, \quad Re = \frac{bx^2}{\nu(1-at)}, \\ \lambda = \frac{Gr}{Re^2}, \quad Ec = \frac{u_w^2}{c_p(T_w - T_\infty)}, \quad Pr = \frac{\nu_f}{\alpha}, \quad Br = \frac{\mu_f u_w^2}{\kappa_f(T_w - T_\infty)}, \\ s = \frac{v_0}{\sqrt{\nu_f b}}, \quad Rd = \frac{4\sigma^* T_\infty^3}{\kappa_f k^*}, \quad E_1 = \frac{E_0}{u_w B_0}, \quad Fr = \frac{c_p}{\sqrt{K^*}}, \\ F = \frac{c_p}{x\sqrt{K^*}}, \quad \alpha^* = \frac{\nu_f(1-at)}{K^* b}. \end{aligned} \quad (25)$$

Appropriate finite values were designated to  $\eta$  concerning the varying values of the problem's parameters. For variables lacking initial values, estimates are defined as initial values. A tolerance of  $10^{-10}$  was also considered for obtaining the solution.

The coefficient of the Nusselt number  $Nu$ , skin friction  $C_f$ , heat flux  $q_w$ , and tangential stress at the sheet  $\tau_w$  are all fundamental numbers, which are stated as

$$q_w = - \left[ \left( \kappa_{hnf} + \frac{16T_\infty^3 \sigma^*}{3k^*} \right) T_y \right]_{y=0}, \quad \tau_w = \mu_{hnf} [U_y]_{y=0} \quad (26)$$

The dimensionless versions of the skin friction factor and the coefficient of heat transmission are as follows:

$$Re^{\frac{1}{2}} C_f = A_1 f''(0), \quad Nu / Re^{\frac{1}{2}} = - \left( A_5 + \frac{4}{3} Rd \right) \theta'(0) \quad (27)$$

The local Reynolds number is denoted by  $Re$ . The empirical formulations and numerical values for the thermo-physical properties of hybrid nano-fluids are shown in Tables 2 and 3, respectively.

**Table 2.** Thermo-physical values of fluid and nano-particles [58].

Physical Properties	Fluid (H <sub>2</sub> O)	Cu (ϕ <sub>1</sub> )	Al <sub>2</sub> O <sub>3</sub> (ϕ <sub>2</sub> )
ρ	997.1	8933	3970
c <sub>p</sub>	4180	385	765
κ	0.613	401	40
β	21	1.67	0.85
σ	0.05	59.6 × 10 <sup>6</sup>	35 × 10 <sup>6</sup>

**Table 3.** Thermo-physical features of hybrid nano-fluids [58].

Properties	Hybrid Nano-Fluid
Density	$\rho_{hnf} = [(1 - \phi_1)\rho_f + \phi_1\rho_{s_1}](1 - \phi_2) + \phi_2\rho_{s_2}$
Viscosity	$\mu_{hnf} = \mu_f(1 - \phi_1)^{-2.5}(1 - \phi_2)^{-2.5}$
Heat capacity	$(\rho c_p)_{hnf} = [(1 - \phi_1)(\rho c_p)_f + \phi_1(\rho c_p)_{s_1}](1 - \phi_2) + ((\rho c_p)_{s_2})\phi_2$
Thermal conductivity	$\kappa_{hnf} = \frac{\kappa_{s_2} + (n-1)\kappa_{nf} + (n-1)\phi_2(\kappa_{nf} - \kappa_{s_2})}{\kappa_{s_2} + (n-1)\kappa_{nf} + \phi_2(\kappa_{nf} - \kappa_{s_2})} \kappa_{nf}$ where $\kappa_{nf} = \frac{\kappa_{s_1} + (n-1)\kappa_f + (n-1)\phi_1(\kappa_f - \kappa_{s_1})}{\kappa_{s_1} + (n-1)\kappa_f + \phi_1(\kappa_f - \kappa_{s_1})} \kappa_f$
Electrical conductivity	$\sigma_{hnf} = \frac{\sigma_{s_2} + (n-1)\sigma_{nf} + (n-1)\phi_2(\sigma_{nf} - \sigma_{s_2})}{\sigma_{s_2} + (n-1)\sigma_{nf} + \phi_2(\sigma_{nf} - \sigma_{s_2})} \sigma_{nf}$ where $\sigma_{nf} = \frac{\sigma_{s_1} + (n-1)\sigma_f + (n-1)\phi_1(\sigma_f - \sigma_{s_1})}{\sigma_{s_1} + (n-1)\sigma_f + \phi_1(\sigma_f - \sigma_{s_1})} \sigma_f$
Thermal expansion coefficient	$(\rho\beta)_{hnf} = [(1 - \phi_1)(\rho\beta)_f + \phi_1(\rho\beta)_{s_1}](1 - \phi_2) + (\rho\beta)_{s_2}\phi_2$

The Matlab BVP4C tool was used to find the numerical solutions. By inserting the appropriate transformations, the governing Equations (1)–(4) and their associated boundary conditions (5) were transformed into the local non-dimensional Equations (16) and (17). To use this technique, each equation is transformed into a set of first-order differential equations as follows.

$$\begin{aligned}
 f &= z(1) \quad , \quad f' = z(2) \quad , \quad f'' = z(3) \quad , \quad f''' = z'(3) \\
 \theta &= z(4) \quad , \quad \theta' = z(5) \quad , \quad \theta'' = z'(5) \\
 z'(3) &= \frac{-A_2}{A_1} \left( z(3)z(1) - z(2)^2(1 + Fr) - \delta \left( \frac{\eta}{2} z(3) + z(2) \right) \right) \\
 &\quad - \frac{1}{A_1} [A_3 M(E_1 - z(2)) + A_4 \lambda z(4) - A_1 \alpha^* z(2)] \\
 z'(5) &= \frac{-A_6 Pr}{\left( A_5 + \frac{4}{3} Rd \right)} \left( z(5)z(1) - z(4)z(2) - \left( \frac{\eta}{2} z(5) + 2z(4) \right) \delta \right) \\
 &\quad - \frac{1}{\left( A_5 + \frac{4}{3} Rd \right)} \left[ A_1 Br z(3)^2 + \frac{A_2 A_5}{A_1} (A z(2) + B z(4)) \right]
 \end{aligned} \tag{28}$$

with bounding condition

$$z_0(1) = s \quad , \quad z_0(2) = 1 \quad , \quad z_0(4) = 1 \quad , \quad z_\infty(2) = 0 \quad , \quad z_\infty(4) = 0 \tag{29}$$

Appropriate finite values are designated to η concerning the varying values of the problem’s parameters. For variables lacking initial values, estimates are defined as initial values. A tolerance of 10<sup>-10</sup> is also considered for obtaining the solution.

#### 4. Entropy Generation

Among the influences of electric and magnetic forces, the expression for the generation number of volumetric entropy is as follows [58]:

$$S'''_{gen} = \frac{\kappa_{lmf}}{T_\infty^2} (T_y)^2 + \frac{\mu_{lmf}}{T_\infty} (U_y)^2 + \frac{\sigma_{lmf}}{T_\infty} (UB - E)^2 \tag{30}$$

All three effects—conduction, viscosity, and joule heating—are accounted for in the preceding equation. The first phrase above shows that heat conduction is irreversible. The second component illustrates the non-reversibility due to frictional effects, while the third term stands for the joule dissipation of the electric and magnetic fields. In its dimensionless version, entropy production reads as follows:

$$Ns = \frac{S'''_{gen}}{S'''_0} = A_5 Re \theta'^2 + A_1 \frac{Br}{\Omega} Re (f'')^2 + A_3 M Re \frac{Br}{\Omega} (f' - E_1)^2 \tag{31}$$

where  $S'''_0 = \frac{k_f(T_w - T_\infty)^2}{x^2 T^2}$  is entropy production rate and  $\Omega = \frac{(T_w - T_\infty)}{T_\infty}$  is a dimensionless temperature ratio.

With these numerical values, we can construct the corresponding correlation equations, which are written as

$$\frac{1}{2} C_f Re^{\frac{1}{2}} = 1.334273 - 0.5150844 E_1 + 0.1322922 \delta + 0.2531761 M \tag{32}$$

$$\frac{Nu}{\sqrt{Re}} = 3.085112 + 1.651553 Rd + 0.7631059 \delta - 0.3885791 Br \tag{33}$$

The equation is valid for  $0 \leq E_1 \leq 0.3$ ,  $0 \leq \delta, Br, Rd \leq 0.6$  and  $0 \leq M \leq 1.5$ .

#### 5. Results and Discussion

In several exceptional circumstances where  $E_1 = 0$ ,  $\delta = 0$ ,  $\lambda = 0$ ,  $\phi_1 = 0$  and  $\phi_2 = 0$ , the skin friction coefficient is compared with that found by Ibrahim and Shankar [59] to evaluate the reliability of the current findings. Table 4 shows that the acquired results are consistent with the prior study. Table 5 shows the local Skin friction and local Nusslet number for different combinations of parameters. The discussion centres on how different factors influence the flow and temperature distributions, as well as the entropy generation number and other vital metrics. We show that the results for a range of parameter values, including  $Pr = 6.2$ ,  $Fr = 0.1$ ,  $\alpha^* = A = B = 0.2$ ,  $Re = 12$ , and  $\Omega^{-1} = 1$ , are held constant. The diagram in Figure 2 illustrates the velocity field  $f'(\eta)$  affected by the electric field parameter, magnetic parameter, mixed convection parameter, unsteadiness parameter, suction/injection parameter, and Forchheimer coefficient. Figure 2a illustrates how the electric field affects velocity. The flow rate above the sheet grew significantly as the  $E_1$  values increased. Because the electric field amplifies the Lorentz force, it acts as an accelerating force and reduces fluid friction. As seen in Figure 2b, the fluid velocity decreases with time due to the magnetic field intensity  $M$ . The resistive type force is physically increased by the magnetic field, and this could control the flow rate. For an explanation of how  $\lambda$  influences the velocity distribution, see Figure 2c. It is seen that  $f'(\eta)$  increases as  $\lambda$  is altered. The temperature difference and buoyancy forces both rise with an increase in the mixed convection parameter, which, in turn, causes the convection to rise and the flow to accelerate. As  $\delta$  values increase, Figure 2d shows that the fluid velocity decreases close to the sheet but increases far from the wall. Because of the decreased stretching rate caused by the unsteadiness factor, the boundary layer's thickness and velocity both decrease. Figure 2e illustrates the predicted effect of the suction/injection parameters over  $(s)$ . The boundary layer becomes thinner and slows down as the suction parameter  $(s > 0)$  increases. The goal of suction is to bring liquid to the surface so that friction with the

solid ground can slow it down. However, with the injection value ( $s < 0$ ), the reverse trend was observed when the injection increased the stream flow. In Figure 2f, a rise in the Forchheimer number  $Fr$  results in a decrease in the size of the velocity field.

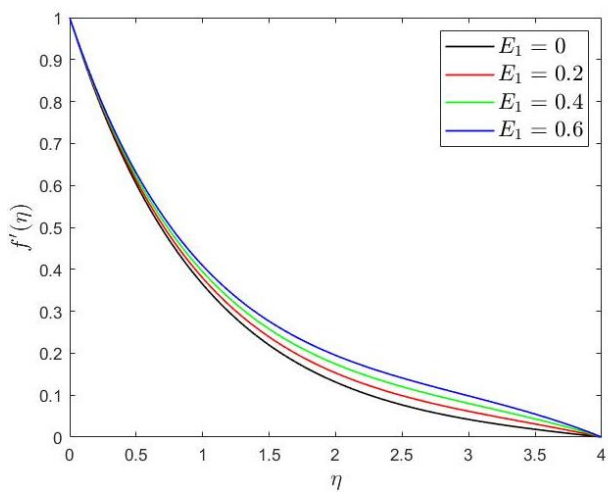
**Table 4.** Computed value of skin friction coefficient.

$s$	$M$	Ref. [59]	Present Study
0	1	1.4142	1.41422
0.2		1.5177	1.51775
0.7		1.8069	1.80688
1		2.0000	2.00000
0.5	0	1.2808	1.28083
	0.5	1.5000	1.50000
	1	1.6861	1.68614
	1.5	1.8508	1.85078
	2	2.0000	2.00000

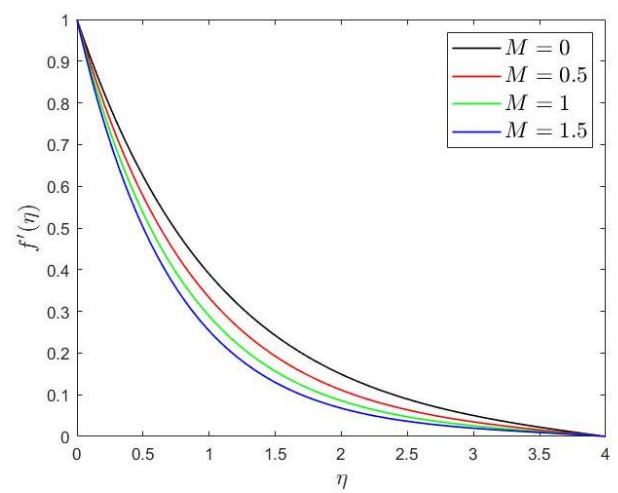
The influence of temperature variation on a set of parameters is shown in Figure 3. Figure 3a shows that, when the Brinkman number  $Br$  rises, so does the fluid temperature. Figure 3b displays the temperature shifts for various radiation parameter values. The figure clearly indicates that  $Rd$  increases the boundary layer's thickness and temperature, that is, the thermal radiation boosts the thermal field inside the system. Figure 3c displays the fluid temperature's response to the unsteadiness parameter and shows a dramatic drop in temperature as the unsteadiness parameter increases.

Figure 3d displays the temperature distribution with respect to the space-dependent heat generation parameter. As the heat source ( $A > 0$ ) values rise, the fluid temperature rises, as predicted; when the heat source ( $A < 0$ ) values decrease, energy is absorbed and the temperature drops. Figure 3e illustrates how temperature-dependent heat source  $B$  affects the heat transfer. As  $B$  increases, the temperature rises as an illustration of energy transmission. Conversely, when heat energy is absorbed, ( $B < 0$ ) values decrease, resulting in a depression close to the boundary layer. As we can see in Figure 3f, the temperature field becomes larger as the Forchheimer number  $Fr$  rises.

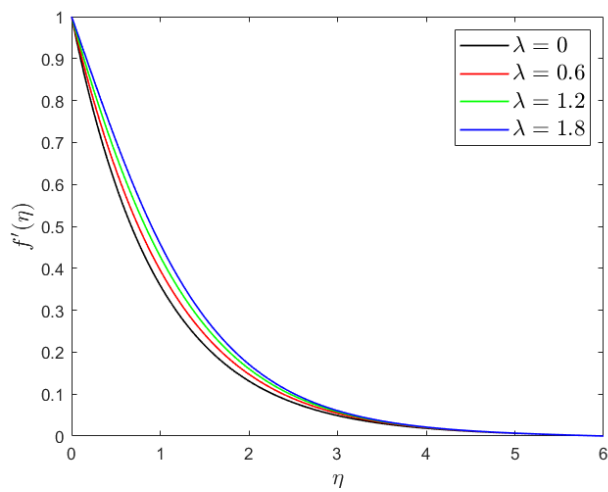
Figure 4 illustrates the effect of significant elements on the entropy generation number  $Ns$ , allowing one to probe the underlying physical aspects of the issue. Figure 4a shows that when  $M$  increases,  $Ns$  increases near the stretching sheet while it changes far away from the sheet. Figure 4b demonstrates the importance of  $Ns$  for various values of the Brinkman number, where a rise in  $Ns$  is shown for larger values of  $Br$ . The underlying physics is that  $Br$  has viscous effects. When  $Br$  increases, the fluid friction becomes the primary cause of entropy formation. Figure 4c depicts  $Ns$  as a function of the Reynolds number, showing how  $Ns$  improved for large values of  $Re$ . This is intuitively true from a physical standpoint since an increase in  $Re$  values leads to agitated motion among the fluid particles, which increases entropy production. At last, Figure 4d shows a schematic of the relationship between  $Ns$  and the temperature ratio parameter  $\Omega^{-1}$ . It pointed out that higher irreversibility occurs when the temperature rises when  $\Omega^{-1}$  has a more significant value.



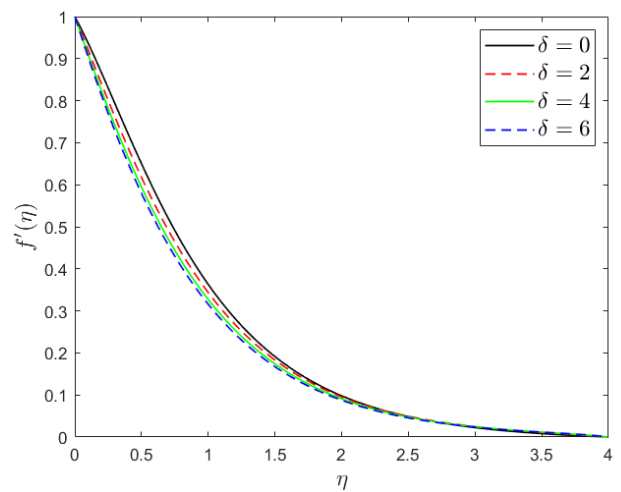
(a) Variations in  $f'(\eta)$  as a result of  $E_1$



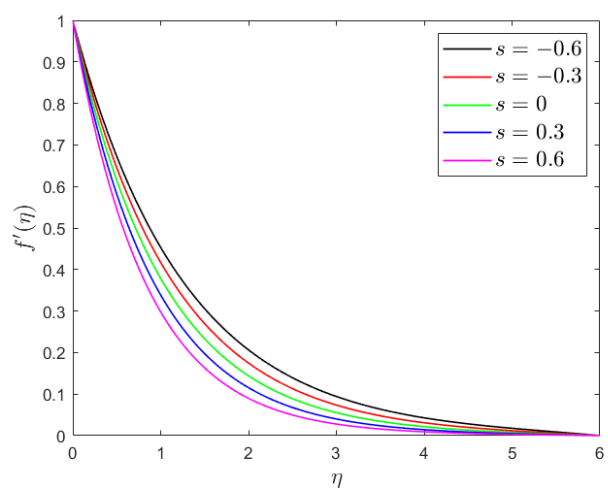
(b) Variations in  $f'(\eta)$  as a result of  $M$



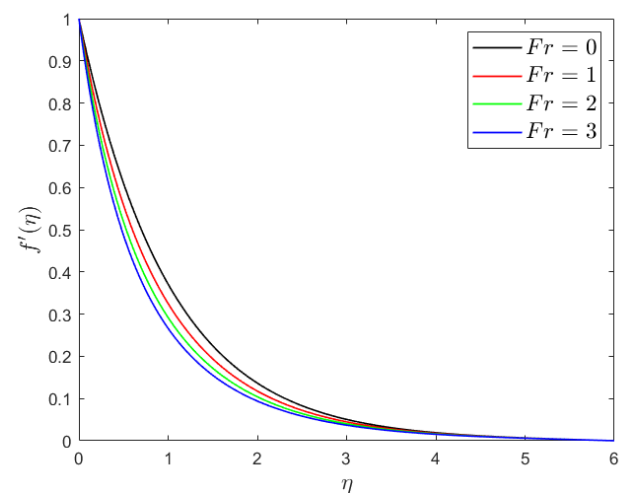
(c) Variations in  $f'(\eta)$  as a result of  $\lambda$



(d) Variations in  $f'(\eta)$  as a result of  $\delta$

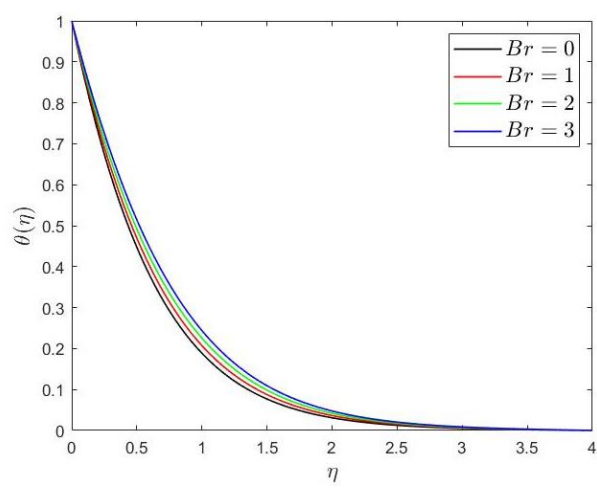


(e) Variations in  $f'(\eta)$  as a result of  $s$

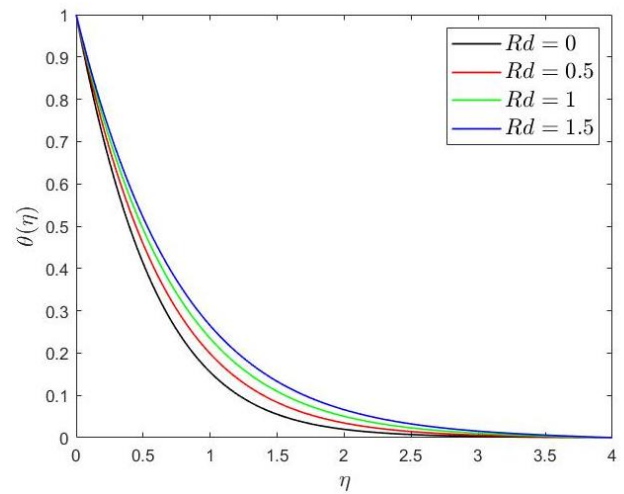


(f) Variations in  $f'(\eta)$  as a result of  $Fr$

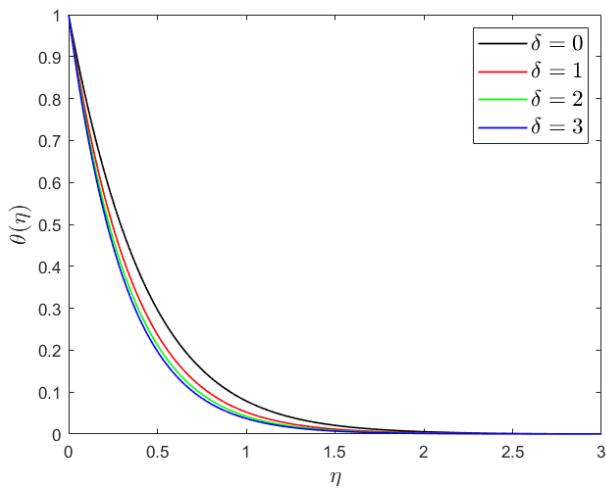
**Figure 2.** Velocity profiles under the impact of novel factors.



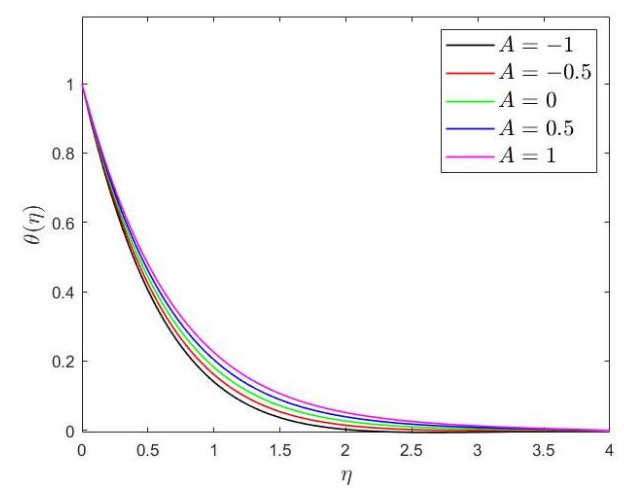
(a) Variations in  $\theta(\eta)$  as a result of  $Br$



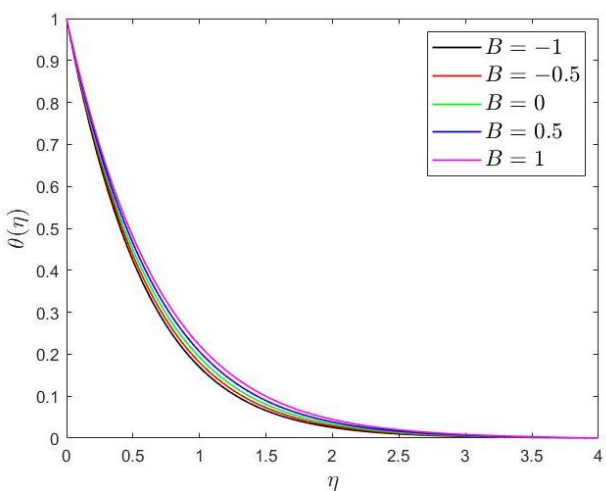
(b) Variations in  $\theta(\eta)$  as a result of  $Rd$



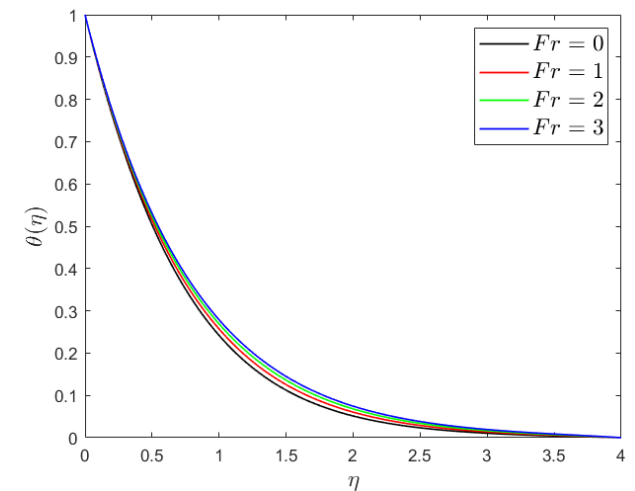
(c) Variations in  $\theta(\eta)$  as a result of  $\delta$



(d) Variations in  $\theta(\eta)$  as a result of  $A$



(e) Variations in  $\theta(\eta)$  as a result of  $B$



(f) Variations in  $\theta(\eta)$  as a result of  $Fr$

**Figure 3.** Temperature profiles under the impact of novel factors.

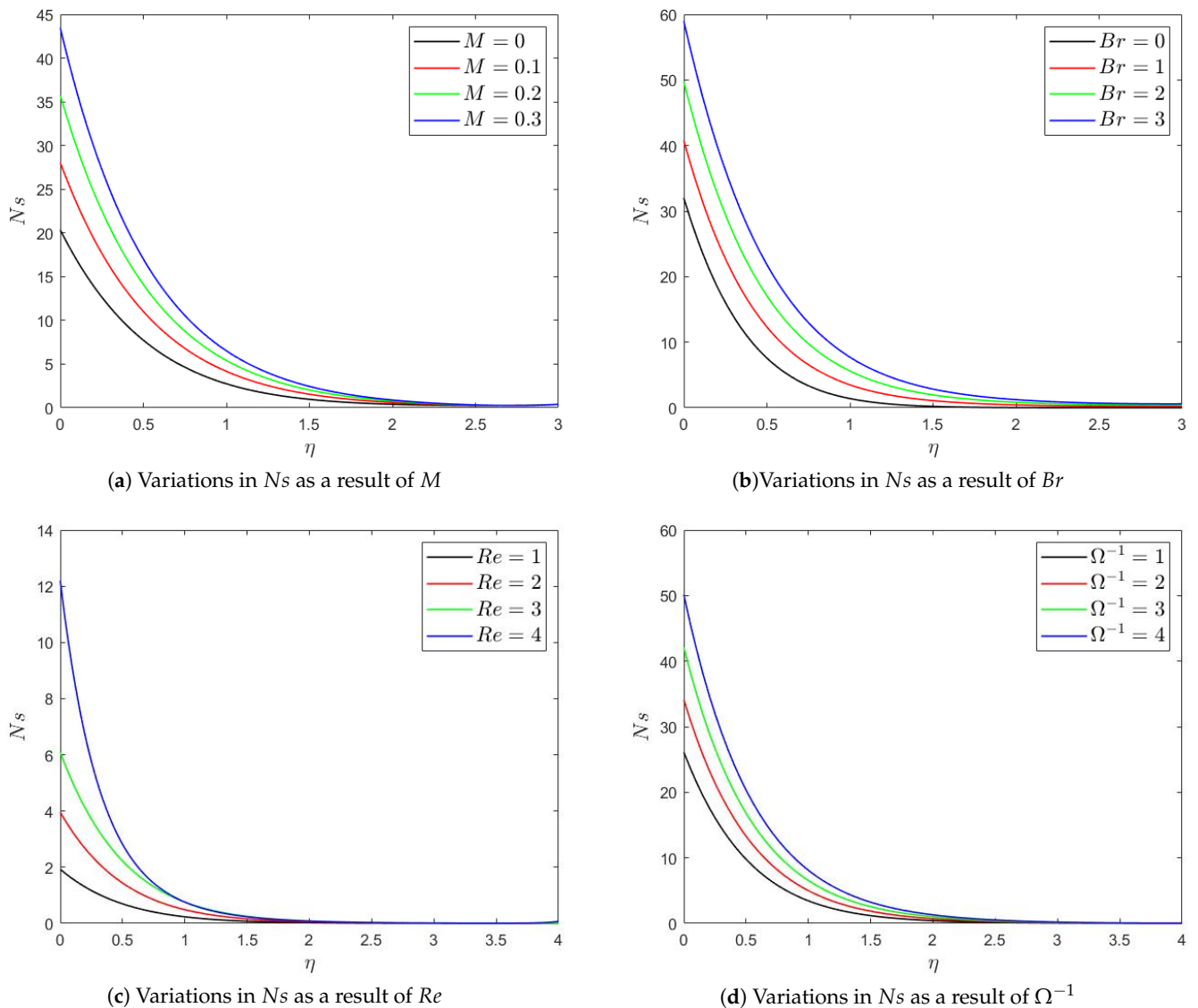
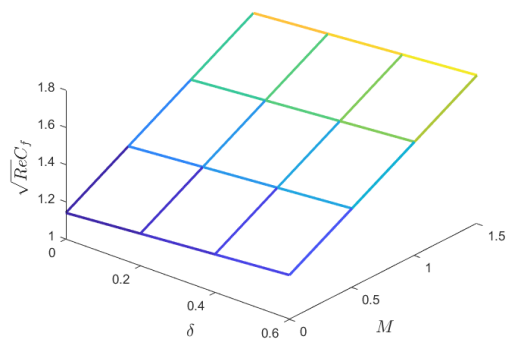
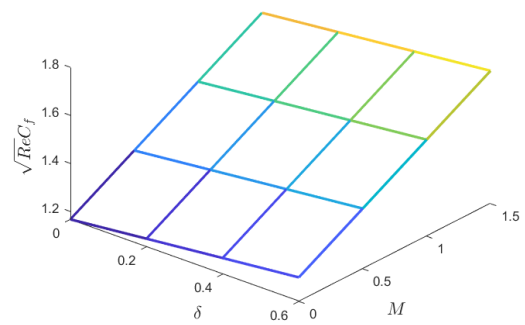


**Figure 4.** Entropy generation under the impact of novel factors.

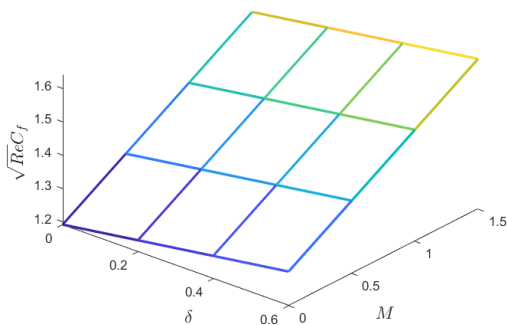
Figure 5 displays the relationship between the skin friction coefficient and the heat transfer rate as a function of the innovative parameters. According to the data, the skin friction coefficient increased with an increase in the magnetic field strength. The most important reason is that strong magnetic effects that increase  $C_f$  create a magnetic field that works against the flow of hybrid nano-fluids across the sheet surface. The electric field parameter had the opposite effect of decreasing it, while the unsteadiness parameter increased it. With larger values of the radiation parameter, as shown in Figure 6, the Nusselt number increases because thermal radiation generates a greater molecular force in the flow. Nonetheless, the Brinkman number trends downward. As the unsteadiness parameter rises, the friction factor and Nusselt number both rise. Figure 7 depicts the percentage increase (or decrease) in the skin friction coefficient and local Nusselt number for the base fluid, nano-fluid, and hybrid nano-fluid, expressed as  $\left(\frac{A-B}{B} \times 100\right)$ . The  $\frac{1}{2}C_f Re^{\frac{1}{2}}$  and  $\frac{Nu}{Re^{\frac{1}{2}}}$  are found to decrease.



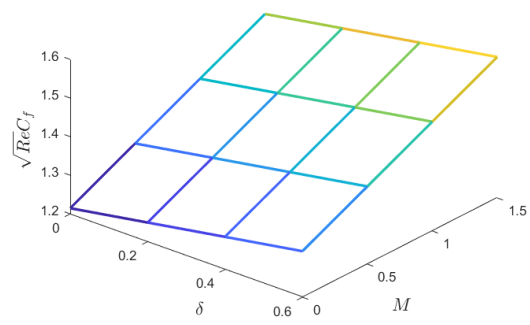
(a) Impact of  $\delta$ ,  $E_1 = 0.1$  on  $Re^{0.5}C_f$



(b) Impact of  $\delta$ ,  $E_1 = 0.2$  on  $Re^{0.5}C_f$

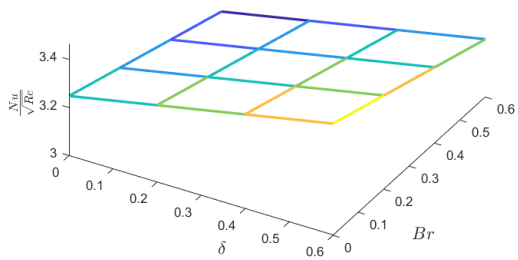


(c) Impact of  $\delta$ ,  $E_1 = 0.3$  on  $Re^{0.5}C_f$

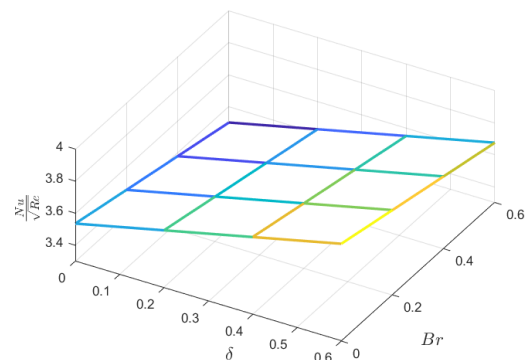


(d) Impact of  $\delta$ ,  $E_1 = 0.4$  on  $Re^{0.5}C_f$

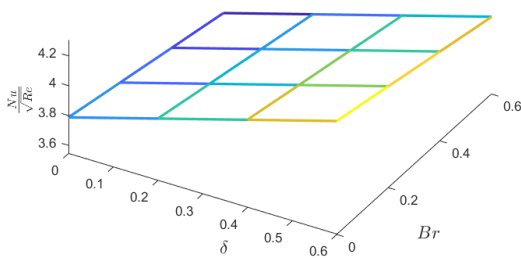
**Figure 5.** Variation in skin friction coefficient  $Re^{\frac{1}{2}}C_f$  for various values of  $\delta$  and  $E_1$ .



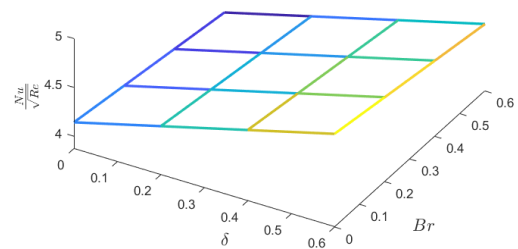
(a) Impact of  $\delta$ ,  $Rd = 0$  on  $Nu/Re^{0.5}$



(b) Impact of  $\delta$ ,  $Rd = 0.2$  on  $Nu/Re^{0.5}$



(c) Impact of  $\delta$ ,  $Rd = 0, 4$  on  $Nu/Re^{0.5}$



(d) Impact of  $\delta$ ,  $Rd = 0.6$  on  $Nu/Re^{0.5}$

**Figure 6.** Variation in Nusselt number  $Nu/Re^{0.5}$  for different values of  $\delta$  and  $Rd$ .

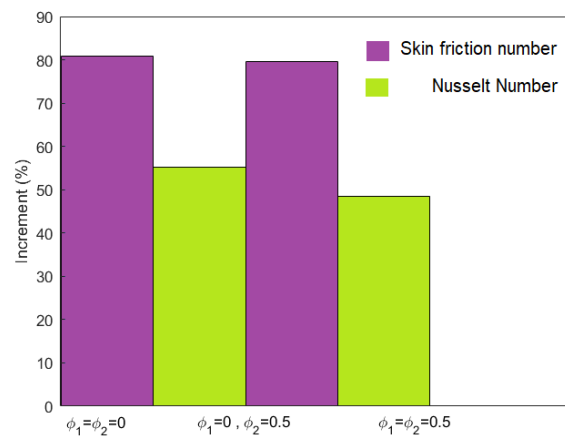


**Figure 7.** Local skin friction number and Nusselt number for base fluid, nano-fluid, and hybrid nano-fluid.

**Table 5.** Local skin friction and local Nusslet number for different combination.

$E_1$	$\delta$	$M$	$C_f \sqrt{Re}$	$Rd$	$\delta$	$Br$	$\frac{Nu}{\sqrt{Re}}$
0	0	0	1.24055	0	0	0	3.15502
		0.5	1.45188			0.2	3.07932
		1	1.63642			0.4	3.00371
		1.5	1.80205			0.6	2.92818
		0.2	0			1.27808	0.2
	0.2	0.5	1.47705	0.2	3.17179		
		1	1.65304	0.4	3.1043		
		1.5	1.81238	0.6	3.03688		
		0.4	0	1.31173	0.4	0	3.31076
		0.5	1.49989	0.2	3.24923		
	0.4	1	1.66818	0.4	3.18776		
		1.5	1.82171	0.6	3.12633		
		0.6	0	1.34213	0.6	0	3.37259
		0.5	1.52078	0.2	3.31573		
		1	1.6821	0.4	3.25891		
0.1	0	1.5	1.83029	0.2	0	0.6	3.20213
		0	1.24055			0	3.44101
		0.5	1.40459			0.2	3.362
		1	1.55522			0.4	3.28308
		1.5	1.69421			0.6	1.24055
	0.2	0	1.27808	0.2	0	3.58856	
		0.5	1.43461	0.2	3.51733		
		1	1.57882	0.4	3.44617		
		1.5	1.7125	0.6	3.37508		
		0.4	0	1.31173	0.4	0	3.71083
	0.4	0.5	1.46144	0.2	3.64531		
		1	1.59988	0.4	3.57985		
		1.5	1.72876	0.6	3.51444		
		0.6	0	1.34213	0.6	0	3.8148
		0.5	1.48566	0.2	3.75371		
0.6	1	1.61888	0.4	3.69265			
	1.5	1.74337	0.6	3.63164			

Table 5. Cont.

$E_1$	$\delta$	$M$	$C_f\sqrt{Re}$	$Rd$	$\delta$	$Br$	$\frac{Nu}{\sqrt{Re}}$
0.2	0	0	1.24055	0.4	0	0	3.69209
		0.5	1.3584			0.2	3.61041
		1	1.47601			0.4	3.52883
		1.5	1.58875			0.6	3.44733
		0.2	0			1.27808	0.2
	0.5	1.39288	0.2	3.82488			
	1	1.506	0.4	3.75076			
	1.5	1.61438	0.6	3.6767			
	0.4	0	1.31173	0.4	0	4.06879	
	0.5	1.42347	0.2		4.00004		
	1	1.53259	0.4		3.93133		
	1.5	1.63711	0.6		3.86268		
	0.6	0	1.34213		0.6	0	4.21217
	0.5	1.45087	0.2	4.14762			
	1	1.55637	0.4	4.0831			
1.5	1.65744	0.6	4.01863				
0.3	0	0	1.24055	0.6		0	0
		0.5	1.31316		0.2		3.83274
		1	1.39851		0.4		3.74893
		1.5	1.48536		0.6		3.66521
		0.2	0		1.27808		0.2
	0.5	1.3518	0.2	4.10367			
	1	1.43441	0.4	4.02707			
	1.5	1.51782	0.6	3.95053			
	0.4	0	1.31173	0.4	0	4.39486	
	0.5	1.38595	0.2		4.32339		
	1	1.4662	0.4		4.25197		
	1.5	1.54665	0.6		4.1806		
	0.6	0	1.34213		0.6	0	4.57545
	0.5	1.41639	0.2	4.50798			
	1	1.49453	0.4	4.76062			
1.5	1.57243	0.6	4.37318				

### 6. Conclusions

A theoretical analysis has been conducted to determine how various governing parameters affect the flow field and heat transfer properties of the EMHD boundary layer motion of a hybrid nano-fluid above a stretching sheet. These include the Brinkman number, the Forchheimer number, the space-dependent coefficient, the temperature-dependent coefficient, the electric parameter, the thermal radiation, the suction parameter, the mixed convection, and the unsteadiness parameters. The numerical results obtained here agree rather well with those found in the literature in a subset of the situations studied. Important conclusions are summed up here.

- Increases in the injection, electric, and mixed convection parameters ( $s < 0$ ) result in increases in the velocity profile. Conversely, as the suction parameter ( $s > 0$ ), unsteadiness parameter, magnetic parameter, and Forchheimer number increase, the velocity decreases.
- The temperature profile amplifies with increments in the Brinkman number ( $Br$ ), thermal radiation ( $Rd$ ), space-dependent heat generation ( $A > 0$ ), temperature-dependent heat generation ( $B > 0$ ), and Forchheimer number ( $Fr$ ). But it shows the reverse behaviour for the unsteadiness parameter ( $\delta$ ), space-dependent heat absorption ( $A < 0$ ), and temperature-dependent heat absorption ( $B < 0$ ).
- The entropy generation is enhanced by increases in the Brinkmann number, magnetic parameter, Reynolds number, and temperature ratio parameter.

- Increases in the skin friction coefficient are caused by increases in the unsteadiness and magnetic parameters. Furthermore, as the electric field parameter increases, the skin friction coefficient decreases.
- The Nusselt number rises with increases in the unsteadiness and thermal radiation parameters. Additionally, as the Brinkman number increases, the Nusselt number decreases.
- This study is useful to thermal science applications in various areas of engineering and technology. Also, the study can be extended with different nano-particles and base fluids to explore the enhancement techniques.
- This study is beneficial to thermal science applications because it discusses the factors that lead to the working hybrid nano-liquid thermal enhancement.

**Author Contributions:** Conceptualisation, S.S.; methodology, N.M.A. and S.S.; software, N.M.A. and S.S.; validation, N.M.A. and S.S.; formal analysis, N.M.A. and S.S.; investigation, N.M.A. and S.S.; writing—original draft preparation, N.M.A. and S.S.; writing—review and editing, N.M.A. and S.S.; visualisation, N.M.A.; supervision, S.S.; All authors have read and agreed to the published version of the manuscript.

**Funding:** This research received no external funding.

**Data Availability Statement:** No data were created.

**Conflicts of Interest:** The authors declare no conflicts of interest.

## References

1. Alizadeh, M.; Dogonchi, A.S.; Ganji, D.D. Micropolar nanofluid flow and heat transfer between penetrable walls in the presence of thermal radiation and magnetic field. *Case Stud. Therm. Eng.* **2018**, *12*, 319–332. [\[CrossRef\]](#)
2. Mondal, H.; Almakki, M.; Sibanda, P. Dual solutions for three-dimensional magnetohydrodynamic nanofluid flow with entropy generation. *J. Comput. Des. Eng.* **2019**, *6*, 657–665. [\[CrossRef\]](#)
3. Parveen, R.; Mahapatra, T. Numerical simulation of MHD double diffusive natural convection and entropy generation in a wavy enclosure filled with nanofluid with discrete heating. *Heliyon* **2019**, *5*, e02496. [\[CrossRef\]](#) [\[PubMed\]](#)
4. Li, Y.-X.; Alshbool, M.H.; Lv, Y.-P.; Khan, I.; Khan, M.R.; Issakhov, A. Heat and mass transfer in MHD Williamson nanofluid flow over an exponentially porous stretching surface. *Case Stud. Therm. Eng.* **2021**, *26*, 100975. [\[CrossRef\]](#)
5. Yu, Y.; Khan, U.; Zaib, A.; Ishak, A.; Waini, I.; Raizah, Z.; Galal, A.M. Exploration of 3D stagnation-point flow induced by nanofluid through a horizontal plane surface saturated in a porous medium with generalized slip effects. *Ain Shams Eng. J.* **2023**, *14*, 101873. [\[CrossRef\]](#)
6. Reddy, N.K.; Sankar, M. Buoyant heat transfer of nanofluids in a vertical porous annulus: A comparative study of different models. *Int. J. Numer. Methods Heat Fluid Flow* **2022**, *33*, 477–509. [\[CrossRef\]](#)
7. Khan, U.; Zaib, A.; Pop, I.; Waini, I.; Ishak, A. MHD flow of a nanofluid due to a nonlinear stretching/shrinking sheet with a convective boundary condition: Tiwari–Das nanofluid model. *Int. J. Numer. Methods Heat Fluid Flow* **2022**, *32*, 3233–3258. [\[CrossRef\]](#)
8. Hayat, T.; Nadeem, S. Heat transfer enhancement with  $Ag\tilde{C}uO$ /water hybrid nanofluid. *Results Phys.* **2017**, *7*, 2317–2324. [\[CrossRef\]](#)
9. Nadeem, S.; Abbas, N.; Khan, A. Characteristics of three dimensional stagnation point flow of Hybrid nanofluid past a circular cylinder. *Results Phys.* **2018**, *8*, 829–835. [\[CrossRef\]](#)
10. Kaska, S.A.; Khalefa, R.A.; Hussein, A.M. Hybrid nanofluid to enhance heat transfer under turbulent flow in a flat tube. *Case Stud. Therm. Eng.* **2019**, *13*, 10039. [\[CrossRef\]](#)
11. Khan, U.; Shafiq, A.; Zaib, A.; Baleanu, D. Hybrid nanofluid on mixed convective radiative flow from an irregular variably thick moving surface with convex and concave effects. *Case Stud. Therm. Eng.* **2020**, *21*, 100660. [\[CrossRef\]](#)
12. Rajesh, V.; Sheremet, M.A.; Öztop, H.F. Impact of hybrid nanofluids on MHD flow and heat transfer near a vertical plate with ramped wall temperature. *Case Stud. Therm. Eng.* **2021**, *28*, 101557. [\[CrossRef\]](#)
13. Mishra, A.; Upreti, H. A comparative study of  $Ag\text{-}MgO$ /water and  $Fe_3O_4\text{-}CoFe_2O_4$ /EG–water hybrid nanofluid flow over a curved surface with chemical reaction using Buongiorno model. *Partial. Differ. Equations Appl. Math.* **2022**, *5*, 100322. [\[CrossRef\]](#)
14. Crane, L.J. Flow past a stretching plate. *Zeitschrift für angewandte Mathematik und Physik ZAMP* **1970**, *21*, 645–647. [\[CrossRef\]](#)
15. Govardhan, K.; Nagaraju, G.; Kaladhar, K.; Balasiddulu, M. MHD and Radiation Effects on Mixed Convection Unsteady Flow of Micropolar Fluid Over A Stretching Sheet. *Procedia Comput. Sci.* **2015**, *57*, 65–76. [\[CrossRef\]](#)
16. Naramgari, S.; Sulochana, C. MHD flow over a permeable stretching/shrinking sheet of a nanofluid with suction/injection. *Alex. Eng. J.* **2016**, *55*, 819–827. [\[CrossRef\]](#)
17. Ibrahim, W. Magnetohydrodynamic (MHD) boundary layer stagnation point flow and heat transfer of a nanofluid past a stretching sheet with melting. *Propuls. Power Res.* **2017**, *6*, 214–222. [\[CrossRef\]](#)

18. Mohammadein, S.A.; Raslan, K.; Abdel-Wahed, M.S.; Abdel-Aal, E.M. KKL-model of MHD CuO-nanofluid flow over a stagnation point stretching sheet with nonlinear thermal radiation and suction/injection. *Results Phys.* **2018**, *10*, 194–199. [[CrossRef](#)]
19. Kho, Y.B.; Hussanan, A.; Mohamed, M.K.A.; Salleh, M.Z. Heat and mass transfer analysis on flow of Williamson nanofluid with thermal and velocity slips: Buongiorno model. *Propuls. Power Res.* **2019**, *8*, 243–252. [[CrossRef](#)]
20. Pal, D.; Mandal, G. Magnetohydrodynamic stagnation-point flow of Sisko nanofluid over a stretching sheet with suction. *Propuls. Power Res.* **2020**, *9*, 408–422. [[CrossRef](#)]
21. Zainal, N.A.; Nazar, R.; Naganthran, K.; Pop, I. Unsteady MHD stagnation point flow induced by exponentially permeable stretching/shrinking sheet of hybrid nanofluid. *Eng. Sci. Technol. Int. J.* **2021**, *24*, 1201–1210. [[CrossRef](#)]
22. Tawade, J.V.; Guled, C.; Noeiaghdam, S.; Fernandez-Gamiz, U.; Govindan, V.; Balamuralitharan, S. Effects of thermophoresis and Brownian motion for thermal and chemically reacting Casson nanofluid flow over a linearly stretching sheet. *Results Eng.* **2022**, *15*, 100448. [[CrossRef](#)]
23. Daniel, Y.S.; Aziz, Z.A.; Ismail, Z.; Salah, F. Impact of thermal radiation on electrical MHD flow of nanofluid over nonlinear stretching sheet with variable thickness. *Alex. Eng. J.* **2018**, *57*, 2187–2197. [[CrossRef](#)]
24. Daniel, Y.S.; Aziz, Z.A.; Ismail, Z.; Salah, F. Thermal radiation on unsteady electrical MHD flow of nanofluid over stretching sheet with chemical reaction. *J. King Saud Univ.-Sci.* **2019**, *31*, 804–812. [[CrossRef](#)]
25. Gopal, D.; Saleem, S.; Jagadha, S.; Ahmad, F.; Almatroud, A.O.; Kishan, N. Numerical analysis of higher order chemical reaction on electrically MHD nanofluid under influence of viscous dissipation. *Alex. Eng. J.* **2020**, *60*, 1861–1871. [[CrossRef](#)]
26. Niranjana, H.; Sivasankaran, S.; Bhuvaneshwari, M. Analytical and numerical study on magnetoconvection stagnation-point flow in a porous medium with chemical reaction, radiation, and slip effects. *Math. Probl. Eng.* **2016**, *2016*, 4017076. [[CrossRef](#)]
27. Sivasankaran, S.; Niranjana, H.; Bhuvaneshwari, M. Chemical reaction, radiation and slip effects on MHD mixed convection stagnation-point flow in a porous medium with convective boundary condition. *Int. J. Numer. Methods Heat Fluid Flow* **2017**, *27*, 454–470. [[CrossRef](#)]
28. Niranjana, H.; Sivasankaran, S.; Bhuvaneshwari, M. Chemical reaction, soot and dufour effects on MHD mixed convection stagnation point flow with radiation and slip condition. *Sci. Iran.* **2017**, *24*, 698–706. [[CrossRef](#)]
29. Sivasankaran, S.; Bhuvaneshwari, M.; Alzahrani, A. Numerical simulation on convection of non-Newtonian fluid in a porous enclosure with non-uniform heating and thermal radiation. *Alex. Eng. J.* **2020**, *59*, 3315–3323. [[CrossRef](#)]
30. Sivasankaran, S.; Bhuvaneshwari, M.; Amer, A. Numerical study on buoyant convection and thermal radiation in a cavity with various thermal sources and Cattaneo–Christov heat flux. *Case Stud. Therm. Eng.* **2021**, *27*, 101207. [[CrossRef](#)]
31. Mallawi, F.; Bhuvaneshwari, M.; Sivasankaran, S.; Eswaramoorthi, S. Impact of double-stratification on convective flow of a non-Newtonian liquid in a Riga plate with Cattaneo–Christov double-flux and thermal radiation. *Ain Shams Eng. J.* **2020**, *12*, 969–981. [[CrossRef](#)]
32. Khashi'ie, N.S.; Waini, I.; Arifin, N.M.; Pop, I. Dual solutions of unsteady two-dimensional electro-magneto-hydrodynamics (EMHD) axisymmetric stagnation-point flow of a hybrid nanofluid past a radially stretching/shrinking Riga surface with radiation effect. *Int. J. Numer. Methods Heat Fluid Flow* **2022**, *33*, 333–350. [[CrossRef](#)]
33. Zainal, N.A.; Nazar, R.; Naganthran, K.; Pop, I. Unsteady stagnation point flow past a permeable stretching/shrinking Riga plate in Al<sub>2</sub>O<sub>3</sub>-Cu/H<sub>2</sub>O hybrid nanofluid with thermal radiation. *Int. J. Numer. Methods Heat Fluid Flow* **2021**, *32*, 2640–2658. [[CrossRef](#)]
34. Bhuvaneshwari, M.; Sivasankaran, S.; Kim, Y.J. Lie Group Analysis of Radiation Natural Convection Flow over An Inclined Surface in a Porous Medium with Internal Heat Generation. *J. Porous Media* **2012**, *15*, 1155–1164 [[CrossRef](#)]
35. Sandeep, N.; Sulochana, C. Dual solutions for unsteady mixed convection flow of MHD micropolar fluid over a stretching/shrinking sheet with non-uniform heat source/sink. *Eng. Sci. Technol. Int. J.* **2015**, *18*, 738–745. [[CrossRef](#)]
36. Karthikeyan, S.; Bhuvaneshwari, M.; Sivanandam, S.; Rajan, S.; Anna University. Erode Arts and Science College Soret and Dufour Effects on MHD Mixed Convection Heat and Mass Transfer of a Stagnation Point Flow towards a Vertical Plate in a Porous Medium with Chemical Reaction, Radiation and Heat Generation. *J. Appl. Fluid Mech.* **2016**, *9*, 1447–1455.
37. Ali, N.; Khan, S.U.; Sajid, M.; Abbas, Z. MHD flow and heat transfer of couple stress fluid over an oscillatory stretching sheet with heat source/sink in porous medium. *Alex. Eng. J.* **2016**, *55*, 915–924. [[CrossRef](#)]
38. Irfan, M.; Khan, M.; Khan, W. Numerical analysis of unsteady 3D flow of Carreau nanofluid with variable thermal conductivity and heat source/sink. *Results Phys.* **2017**, *7*, 3315–3324. [[CrossRef](#)]
39. Cheong, H.T.; Sivasankaran, S.; Bhuvaneshwari, M. Natural convection in a wavy porous cavity with sinusoidal heating and internal heat generation. *Int. J. Numer. Methods Heat Fluid Flow* **2017**, *27*, 287–309. [[CrossRef](#)]
40. Khan, M.; Irfan, M.; Khan, W. Impact of heat source/sink on radiative heat transfer to Maxwell nanofluid subject to revised mass flux condition. *Results Phys.* **2018**, *9*, 851–857. [[CrossRef](#)]
41. Ragupathi, P.; Hakeem, A.A.; Al-Mdallal, Q.M.; Ganga, B.; Saranya, S. Non-uniform heat source/sink effects on the three-dimensional flow of Fe<sub>3</sub>O<sub>4</sub>/Al<sub>2</sub>O<sub>3</sub> nanoparticles with different base fluids past a Riga plate. *Case Stud. Therm. Eng.* **2019**, *15*, 100521. [[CrossRef](#)]
42. Agrawal, P.; Dadheech, P.K.; Jat, R.N.; Bohra, M.; Nisar, K.S.; Khan, I. Lie similarity analysis of MHD flow past a stretching surface embedded in porous medium along with imposed heat source/sink and variable viscosity. *J. Mater. Res. Technol.* **2020**, *9*, 10045–10053. [[CrossRef](#)]
43. Chu, Y.-M.; Ramzan, M.; Shaheen, N.; Chung, J.D.; Kadry, S.; Howari, F.; Malik, M.; Ghazwani, H.A.S. Analysis of Newtonian heating and higher-order chemical reaction on a Maxwell nanofluid in a rotating frame with gyrotactic microorganisms and variable heat source/sink. *J. King Saud Univ.-Sci.* **2021**, *33*, 101645. [[CrossRef](#)]

44. Bhuvanewari, M.; Sivasankaran, S.; Malarselvi, A.; Ganga, B. Radiation and cross diffusion on unsteady chemically reactive convective flow through an extended surface in heat generating porous medium. *Int. J. Energy Technol. Policy* **2021**, *17*, 494–509. [[CrossRef](#)]
45. Yesodha, P.; Bhuvanewari, M.; Sivasankaran, S.; Saravanan, K. Nanofluid flow with activation energy and heat generation under slip boundary condition with convective heat and mass transfer. *Mater. Today Proc.* **2022**, *59*, 959–967. [[CrossRef](#)]
46. Gautam, A.K.; Rajput, S.; Bhattacharyya, K.; Pandey, A.K.; Chamkha, A.J.; Begum, M. Comparative study of two non-Newtonian fluids with bioconvective induced MHD flow in presence of multiple slips, heat source/sink and nonlinear thermal radiation. *Chem. Eng. J. Adv.* **2022**, *12*, 100365. [[CrossRef](#)]
47. Bejan, A. A Study of Entropy Generation in Fundamental Convective Heat Transfer. *J. Heat Transf.* **1979**, *101*, 718–725. [[CrossRef](#)]
48. Bejan, A. The thermodynamic design of heat and mass transfer processes and devices. *Int. J. Heat Fluid Flow* **1987**, *8*, 258–276. [[CrossRef](#)]
49. Goqo, S.; Olonijju, S.; Mondal, H.; Sibanda, P.; Motsa, S. Entropy generation in MHD radiative viscous nanofluid flow over a porous wedge using the bivariate spectral quasi-linearization method. *Case Stud. Therm. Eng.* **2018**, *12*, 774–788. [[CrossRef](#)]
50. Ijaz, M.; Ayub, M.; Khan, H. Entropy generation and activation energy mechanism in nonlinear radiative flow of Sisko nanofluid: Rotating disk. *Heliyon* **2019**, *5*, e01863. [[CrossRef](#)]
51. Abbas, Z.; Naveed, M.; Hussain, M.; Salamat, N. Analysis of entropy generation for MHD flow of viscous fluid embedded in a vertical porous channel with thermal radiation. *Alex. Eng. J.* **2020**, *59*, 3395–3405. [[CrossRef](#)]
52. Usman; Ghaffari, A.; Mustafa, I.; Muhammad, T.; Altaf, Y. Analysis of entropy generation in a power-law nanofluid flow over a stretchable rotatory porous disk. *Case Stud. Therm. Eng.* **2021**, *28*, 101370. [[CrossRef](#)]
53. Ibrahim, W.; Gamachu, D.; Bedada, B. Entropy generation analysis of three dimensional mixed convection flow of couple stress nanofluid with non-Fourier's heat and non-Fick's mass flux model. *Alex. Eng. J.* **2022**, *61*, 8843–8857. [[CrossRef](#)]
54. Alzahrani, A.K.; Sivasankaran, S.; Bhuvanewari, M. Numerical Simulation on Convection and Thermal Radiation of Casson Fluid in an Enclosure with Entropy Generation. *Entropy* **2020**, *22*, 229. [[CrossRef](#)]
55. Sivanandam, S.; Chamkha, A.J.; Mallawi, F.O.M.; Alghamdi, M.S.; Alqahtani, A.M. Effects of Entropy Generation, Thermal Radiation and Moving-Wall Direction on Mixed Convective Flow of Nanofluid in an Enclosure. *Mathematics* **2020**, *8*, 1471. [[CrossRef](#)]
56. Agrawal, R.; Kaswan, P. Entropy generation minimization of Ag-Fe<sub>3</sub>O<sub>4</sub>/water-ethylene glycol squeezed hybrid nanofluid flow between parallel disks. *Int. J. Numer. Methods Heat Fluid Flow* **2022**, *33*, 65–95. [[CrossRef](#)]
57. Bai, Y.; Fang, H.; Zhang, Y. Entropy generation analysis on unsteady flow of Maxwell nanofluid over the stretched wedge with Cattaneo-Christov double diffusion. *Int. J. Numer. Methods Heat Fluid Flow* **2021**, *32*, 2198–2220. [[CrossRef](#)]
58. Mumraiz, S.; Ali, A.; Awais, M.; Shutaywi, M.; Shah, Z. Entropy generation in electrical magnetohydrodynamic flow of Al<sub>2</sub>O<sub>3</sub>-Cu/H<sub>2</sub>O hybrid nanofluid with non-uniform heat flux. *J. Therm. Anal. Calorim.* **2020**, *143*, 2135–2148. [[CrossRef](#)]
59. Ibrahim, W.; Shankar, B. MHD boundary layer flow and heat transfer of a nanofluid past a permeable stretching sheet with velocity, thermal and solutal slip boundary conditions. *Comput. Fluids* **2013**, *75*, 1–10. [[CrossRef](#)]

**Disclaimer/Publisher's Note:** The statements, opinions and data contained in all publications are solely those of the individual author(s) and contributor(s) and not of MDPI and/or the editor(s). MDPI and/or the editor(s) disclaim responsibility for any injury to people or property resulting from any ideas, methods, instructions or products referred to in the content.